



HAL
open science

A Deconvolution Method for the Mapping of Residual Stresses by X-Ray Diffraction

P. Tajdary, L. Morin, C. Braham, G. Gonzalez

► **To cite this version:**

P. Tajdary, L. Morin, C. Braham, G. Gonzalez. A Deconvolution Method for the Mapping of Residual Stresses by X-Ray Diffraction. *Experimental Mechanics*, 2022, 62 (8), pp.1349-1362. 10.1007/s11340-022-00839-5 . hal-04078515

HAL Id: hal-04078515

<https://hal.science/hal-04078515>

Submitted on 23 Apr 2023

HAL is a multi-disciplinary open access archive for the deposit and dissemination of scientific research documents, whether they are published or not. The documents may come from teaching and research institutions in France or abroad, or from public or private research centers.

L'archive ouverte pluridisciplinaire **HAL**, est destinée au dépôt et à la diffusion de documents scientifiques de niveau recherche, publiés ou non, émanant des établissements d'enseignement et de recherche français ou étrangers, des laboratoires publics ou privés.

A Deconvolution Method for the Mapping of Residual Stresses by X-Ray Diffraction

P. Tajdary¹ · L. Morin¹  · C. Braham¹ · G. Gonzalez²

Abstract

Background Inherent averaging effects in X-ray diffraction measurement of residual stresses, related to the finite size of the irradiated area, lead to inaccurate measurements in the presence of high surface stress gradients.

Objective This paper develops a reconstruction method which allows the mapping of heterogeneous residual stresses from X-ray diffraction averaged measurements.

Methods The stress reconstruction is based on a deconvolution of the average XRD measurements. The combination of a fine measurement grid and the use of two collimators lead to an overdetermined linear system on the average stress measured experimentally whose inversion provides the values of the local stress field.

Results First, the method is successfully assessed in a reference problem solved by FEM in which the local distribution and average datasets are known. Then, it is applied to the reconstruction of residual stress mapping from experimental XRD measurements of a specimen processed by repetitive corrugation and straightening. The reconstructed field is in agreement with numerical (local) results of the process.

Conclusion The method developed in this work permits the reconstruction of accurate distributions of heterogeneous near-surface residual-stresses.

Keywords X-ray diffraction · Residual stresses · Aluminum alloys · Severe plastic deformation · Deconvolution

Introduction

The durability of structural components is considerably influenced by residual stresses. The understanding of residual stresses and their determination are thus necessary during the design and manufacturing of products [1, 2], as undesirable tensile residual stresses can decrease fatigue life and corrosion resistance [3]. The origin of residual stresses is the presence of an incompatible strain field, which can be due to heterogeneous plastic deformation or phase transition. Compressive residual stresses can thus be introduced on purpose to improve durability, using for instance shot

peening [4] or laser shock peening [5]. Uncontrolled residual stresses can be introduced unintentionally in most manufacturing processes based on plastic deformation or heat treatment, such as in machining [6], welding [7], severe plastic deformation [8] and additive manufacturing [9], among others. The assessment of residual stress distributions is thus of paramount importance for the durability and reliability of engineering components.

X-ray diffraction (XRD) is a high accuracy and non-destructive method to measure residual stresses in crystalline materials [10]. It is based on the measurement of the shift of the Bragg angle which allows the calculation of the change in interatomic lattice spacing, leading to an estimation of the strain in a small volume under the specimen surface; crystalline planes are thus used as strain gauges [11]. Residual stresses can then be deduced from the elastic theory provided that the X-ray elastic constants are known. In metallic alloys, this method allows measurements in outer layers due to the high absorption of X-rays. Hence, it is generally used to determine (destructively) stress gradients in depth with a very good precision using successive polishing.

✉ L. Morin
leo.morin@ensam.eu

¹ PIMM, Arts et Metiers Institute of Technology, CNRS, Cnam, HESAM University, 151 boulevard de l'Hopital, 75013 Paris, France

² Instituto de Investigaciones en Materiales, Universidad Nacional Autónoma de México, Circuito Exterior S/N, Cd. Universitaria, 04510 México City, Mexico

Alternatively, multi-reflection grazing-incidence techniques allow the determination of depth-dependent stress profiles non-destructively [12, 13].

Nonetheless, an important drawback of X-ray diffraction is the inherent averaging effects of the method which can lead to inaccurate measurement results in the presence of high surface stress gradients [14–17]. Indeed, X-ray diffraction measurements provide the average lattice strain within the irradiated area, whose size depends on the collimator. Therefore, when the characteristic length of the surface strain gradient is smaller than the irradiated area, the corresponding stresses obtained from XRD is an average of the local heterogeneous stresses. The averaging effect can be decreased by using a small irradiated area, but since the diffracting volume has to contain a sufficient number of crystallites to be statistically representative, it cannot be reduced below some critical value in typical engineering materials containing micron-sized crystallites. Consequently, important averaging effects on the residual stresses measured by XRD are expected in the presence of high lateral stress gradients.

Recently, Morin et al. [17] proposed a method to reconstruct spatially the local residual stress field using several X-ray diffraction measurements performed on a regular grid (e.g. using an automatic robot) and with the use of two collimator sizes (inducing two different irradiated areas). Since the average stress obtained from XRD corresponds to the convolution of the local stress, a linear relationship between the point-wise values of the (unknown) local stress field and that of the average stress determined experimentally can be constructed. The inversion of this linear system leads to the so-called *deconvolution* of the residual stress field. The use of a fine measurement grid together with two datasets for the averages make the linear system overdetermined which improves the reconstruction. Their method has been successfully applied to the reconstruction of line stress profiles in a specimen processed by repetitive corrugation and straightening.

The method developed by Morin et al. [17] was based on several hypotheses, the most restrictive one being that the lateral stress-gradients are supposed to occur in only one direction. Hence, this method is restricted by essence to the reconstruction of stress line profiles. The aim of this work is to extend Morin et al. [17]'s reconstruction method to a two-dimensionnal case, which would allow the reconstruction of local heterogeneous residual stress mapping. The paper is organized as follows. In "[A 2D Deconvolution Method of Spatial Residual Stresses Using X-ray Diffraction Measurements](#)", the deconvolution method of Morin et al. [17] is extended to the two-dimensional case. The method is applied in "[Application to the Reconstruction of Local Residual Stress Maps from Simulation Results](#)" to the reconstruction of local residual stresses in a reference case

of repetitive corrugation and straightening in which the local stress field is computed numerically by the finite element method. Finally, in "[Application to the Reconstruction of Local Residual Stress Maps from X-ray Diffraction Measurements](#)", the method is applied to the mapping of residual stresses using experimental data collected on a specimen processed by severe plastic deformation.

A 2D Deconvolution Method of Spatial Residual Stresses Using X-ray Diffraction Measurements

Averaging Effects of X-ray Diffraction Measurements

The components of the stress tensor that are obtained from XRD measurements result from a convolution of the local stress tensor components over the *irradiated area*¹ which is generally of circular or rectangular shape in practical laboratory facilities. In the following, we will make several assumptions which will allow the derivation of a deconvolution method that can be used for practical applications: (i) the irradiated area is square-shaped and (ii) the averaging over the irradiated area is uniform (penumbra effects are disregarded).

Therefore, X-ray diffraction is assumed to consist in the (homogeneous) convolution of the local stress over the irradiated square-shape area, which corresponds to a 2D moving average. Let us consider one component of the stress tensor, or a linear combination of several components (since the convolution applies to each component separately), which is denoted by $\sigma(x, y)$ for convenience, where x and y denotes the spatial coordinates. If the size of irradiated area is denoted by $2a \times 2a$, the moving average $\Sigma^a(x, y)$ of the stress σ is then given by the formula

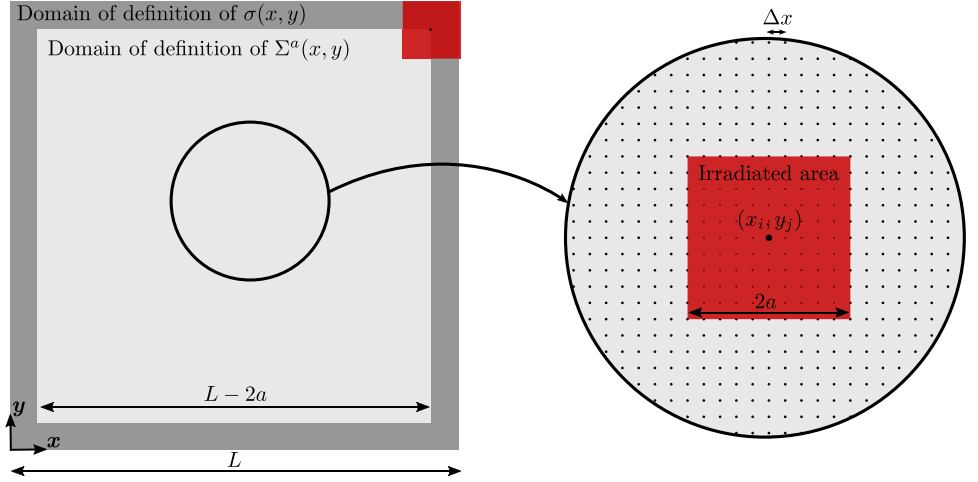
$$\Sigma^a(x, y) = \frac{1}{4a^2} \int_{x-a}^{x+a} \int_{y-a}^{y+a} \sigma(x_1, x_2) dx_1 dx_2. \quad (1)$$

The problem we are addressing is the reconstruction of the local stress field $\sigma(x, y)$ in a 2D domain from the knowledge of its average $\Sigma^a(x, y)$.

Principles of 2D Residual Stress Mapping Reconstruction

The 2D domain considered is a square domain of size $[0, L] \times [0, L]$. The determination of residual stress mapping requires the measurement of the moving average $\Sigma(x, y)$ on a

Fig. 1 Description of the geometry considered for 2D XRD mapping with a square irradiated area



regular grid (see Fig. 1); the domain $[0, L] \times [0, L]$ is discretized onto a uniform grid with spatial scale $\Delta x = \Delta y = L/(N - 1)$, where the total number of points is $N \times N$. We use the following notation: $x_i = (i - 1)\Delta x$, $y_j = (j - 1)\Delta x$, $\sigma_{ij} = \sigma(x_i, y_j)$, with $i = 1, \dots, N$ and $j = 1, \dots, N$. We denote by σ the $N \times N$ matrix that contains the values σ_{ij} .

For simplicity, we assume that the half-width of the irradiated zone is of the form

$$a = k_a \Delta x, \quad (2)$$

where k_a is a positive integer. From the definition of the moving average $\Sigma^a(x, y)$, it is readily seen that it is only defined in the domain $[a, L - a] \times [a, L - a]$. Therefore, on the discretized grid, it reads $\Sigma_{ij}^a = \Sigma^a(x_i, y_j)$ with $i = k_a + 1, \dots, N - k_a$. The matrix Σ^a which contains these values is thus of size $(N - 2k_a) \times (N - 2k_a)$.

Then, the integral defined by equation (1) is approximately calculated using a trapezoidal rule:

$$\begin{aligned} \Sigma_{ij}^a &= \frac{1}{16k_a^2} (\sigma_{i-k_a, j-k_a} + \sigma_{i-k_a, j+k_a} + \sigma_{i+k_a, j-k_a} + \sigma_{i+k_a, j+k_a}) \\ &+ \frac{1}{8k_a^2} \left(\sum_{l=i-k_a+1}^{i+k_a-1} (\sigma_{lj-k_a} + \sigma_{lj+k_a}) + \sum_{m=j-k_a+1}^{j+k_a-1} (\sigma_{i-k_a, m} + \sigma_{i+k_a, m}) \right) \\ &+ \frac{1}{4k_a^2} \sum_{l=i-k_a+1}^{i+k_a-1} \sum_{m=j-k_a+1}^{j+k_a-1} \sigma_{lm}. \end{aligned} \quad (3)$$

In order to establish a linear relation between Σ^a and σ , we introduce a vector representation of these matrices, respectively denoted by $\hat{\Sigma}^a$ and $\hat{\sigma}$ and defined as

$$\hat{\sigma}_{(i-1)N+j} = \sigma_{ij}, \quad \forall i = 1, \dots, N \quad \text{and} \quad j = 1, \dots, N, \quad (4)$$

$$\hat{\Sigma}_{(i-1)(N-k_a)+j}^a = \Sigma_{ij}^a, \quad \forall i = 1, \dots, N - 2k_a \quad \text{and} \quad j = 1, \dots, N - 2k_a. \quad (5)$$

Using this vector representation, the linear relation between Σ^a and σ , defined by equation (3), reads

$$\hat{\Sigma}^a = \mathbf{R}^a \cdot \hat{\sigma} \quad (6)$$

where \mathbf{R}^a is a matrix of size $(N - 2k_a)^2 \times N^2$ which can be constructed from equation (3). For illustrative purposes, the non-zero components of the line number $(i - 1)(N - k_a) + j$ of \mathbf{R}^a , associated with the calculation of the average Σ_{ij}^a , are given by

$$R_{(i-1)(N-k_a)+j, l} = \begin{cases} \frac{1}{16k_a^2} & \text{if } l = (i \pm k_a - 1)(N - k_a) + j \pm k_a \\ \frac{1}{8k_a^2} & \text{if } l = \begin{cases} mN + j \pm k_a \\ (i \pm k_a - 1)(N - k_a) + n \end{cases} \\ \frac{1}{4k_a^2} & \text{if } l = mN + n \\ 0 & \text{otherwise,} \end{cases} \quad (7)$$

where m and n take the values

$$m = i - k_a + 1, \dots, i + k_a - 1, \quad n = j - k_a + 1, \dots, j + k_a - 1. \quad (8)$$

The linear system defined by equation (6) is underdetermined because there are fewer equations $((N - 2k_a)^2)$ than unknowns (N^2) ; the rank of \mathbf{R}^a is necessarily lower than N^2 . Therefore, only an approximate solution of the system can be found, for instance by minimizing the residual sum-of-square. In that case the solution of the minimization problem leads to

$$\hat{\sigma} = (\mathbf{R}^a)^+ \cdot \hat{\Sigma}^a, \quad (9)$$

where $(\mathbf{R}^a)^+$ is the classical Moore-Penrose right pseudoinverse matrix of \mathbf{R}^a defined as

$$(\mathbf{R}^a)^+ = (\mathbf{R}^a)^T \cdot (\mathbf{R}^a \cdot (\mathbf{R}^a)^T)^{-1}. \quad (10)$$

As explained in [17], the reconstructed stress field $\hat{\sigma}$ provided by equation (9) is expected to be inaccurate due to the underdetermined nature of the system as well as the presence of experimental noise on Σ^a . In order to improve the prediction of the residual stress field, it is proposed to (i) construct a smooth estimate $\tilde{\Sigma}^a$ and (ii) use several sets of measurements with different collimators (inducing different diffraction areas).

First, the smooth estimate $\tilde{\Sigma}^a$ is constructed using the robust spline-based smoother developed by [18], based on the minimization of a functional that balances the fidelity to the data, through the residual sum-of-squares (RSS), and the smoothness of the estimate through a penalty term (that depends on the second derivative of the function). The advantage of this approach is that the smooth estimate is unique using the classical method of generalized cross-validation (GCV) which provides the best smoothing parameter avoiding over- or under-smoothing. The details of the smoothing procedure are provided in Appendix 1.

Then, several sets of measurements using different collimators are considered. This permits to increase the number of equations involved in the linear system and ultimately this will improve the accuracy of the reconstructed residual stress field. For illustrative purposes, we consider two sets of measurements associated with two collimators but the extension to an arbitrary number of sets ($n \geq 2$) is straightforward. The irradiated areas have respectively a width denoted by

$2a_1 = 2k_1 \Delta x$ and $2a_2 = 2k_2 \Delta x$, and the associated moving averages $\Sigma^{a_i}(x, y)$ of the stress σ are then given by the formula

$$\Sigma^{a_i}(x, y) = \frac{1}{4a_i^2} \int_{x-a_i}^{x+a_i} \int_{y-a_i}^{y+a_i} \sigma(x_1, x_2) dx_1 dx_2, \quad i = [1, 2]. \quad (11)$$

After smoothing, this leads to the linear relations

$$\hat{\Sigma}^{a_1} = \mathbf{R}^{a_1} \cdot \hat{\sigma}, \quad \hat{\Sigma}^{a_2} = \mathbf{R}^{a_2} \cdot \hat{\sigma}, \quad (12)$$

where the matrices \mathbf{R}^{a_1} and \mathbf{R}^{a_2} are constructed using (7). We denote by $\hat{\Sigma}$ the vector (of length $((N - 2k_{a_1})^2 + (N - 2k_{a_2})^2)$) which concatenates the vectors $\hat{\Sigma}^{a_1}$ and $\hat{\Sigma}^{a_2}$, and by \mathbf{R} the matrix (of size $[(N - 2k_{a_1})^2 + (N - 2k_{a_2})^2] \times N^2$) which concatenates the matrices \mathbf{R}^{a_1} and \mathbf{R}^{a_2} :

$$\hat{\Sigma} = \begin{bmatrix} \hat{\Sigma}^{a_1} \\ \hat{\Sigma}^{a_2} \end{bmatrix}, \quad \mathbf{R} = \begin{bmatrix} \mathbf{R}^{a_1} \\ \mathbf{R}^{a_2} \end{bmatrix}. \quad (13)$$

Using equations (12) and (13), the linear system constructed from the two sets of measurements simply reads

$$\hat{\Sigma} = \mathbf{R} \cdot \hat{\sigma}. \quad (14)$$

Two cases need to be distinguished to find the solution $\hat{\sigma}$:

- If the system is underdetermined (i.e. the rank of \mathbf{R} is lower than N^2), the approximate solution is given, as in

Fig. 2 Geometrical model considered for the repetitive corrugation and straightening simulation

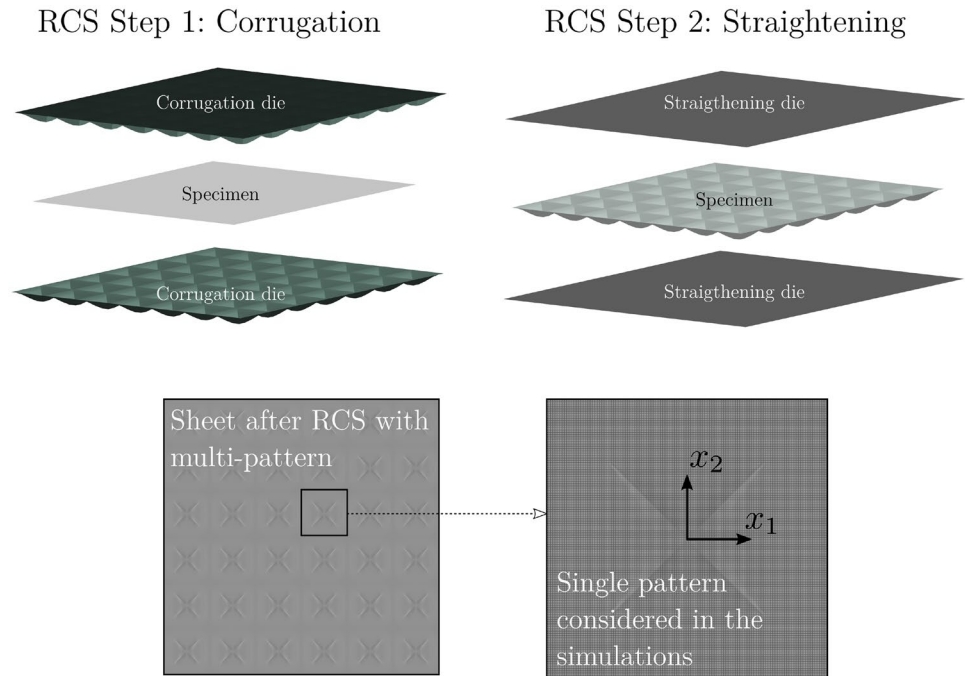


Table 1 Material parameters for the 6061 aluminum alloy used for RCS simulation

Material	E (GPa)	ν	σ_0 (MPa)	h (MPa)	n
AA 6061	69	0.33	160	170	0.3

"Principles of 2D residual stress mapping reconstruction", by

$$\hat{\sigma} = \mathbf{R}^+ \cdot \hat{\Sigma}, \quad (15)$$

where \mathbf{R}^+ is the classical Moore-Penrose right pseudoinverse matrix of \mathbf{R} defined as

$$\mathbf{R}^+ = \mathbf{R}^T (\mathbf{R}\mathbf{R}^T)^{-1}. \quad (16)$$

- If the system is overdetermined (i.e. the rank of \mathbf{R} is equal to N^2), the approximate solution is given by

$$\hat{\sigma} = \mathbf{R}^+ \cdot \hat{\Sigma}, \quad (17)$$

where \mathbf{R}^+ is the classical Moore-Penrose left pseudoinverse matrix of \mathbf{R} defined as

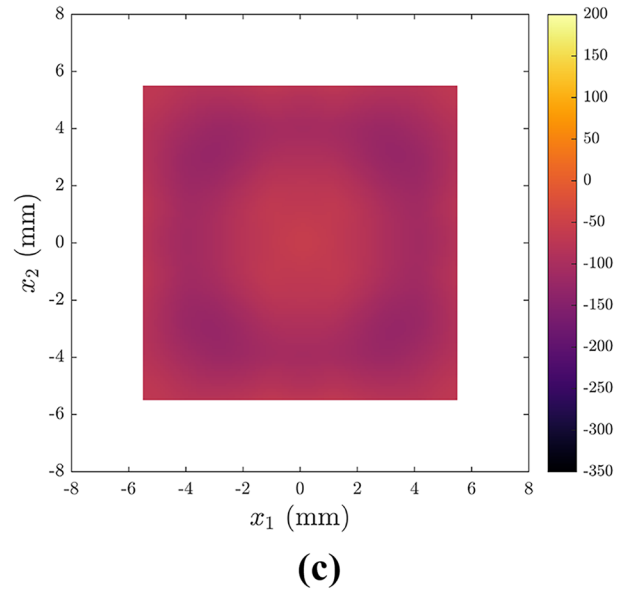
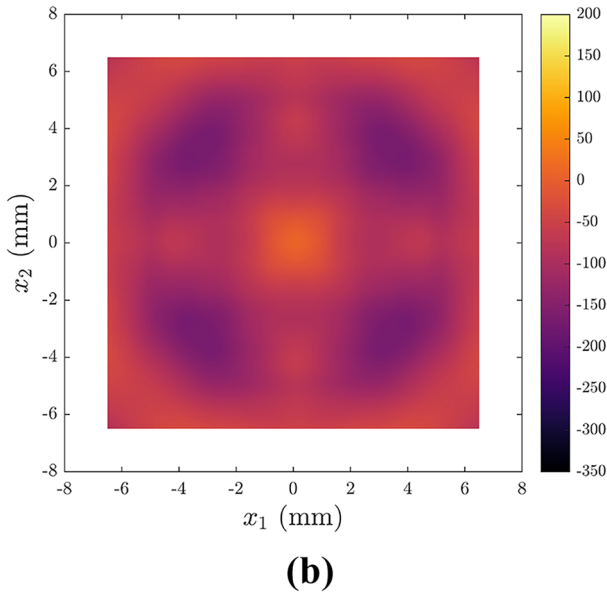
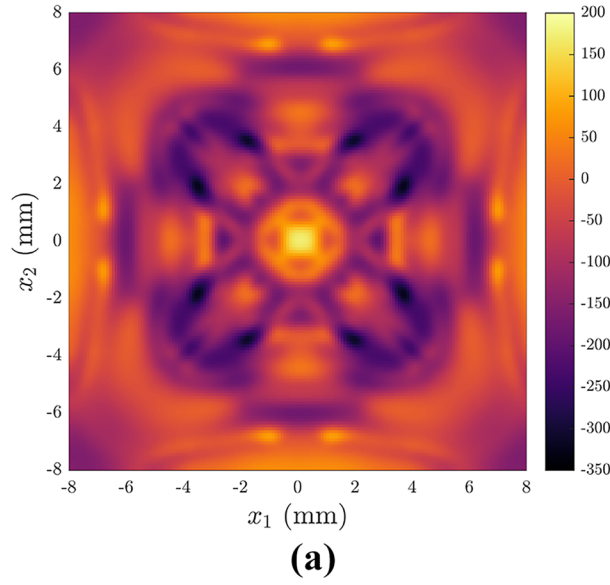


Fig. 3 Results from the numerical simulation of RCS on the bottom surface of the specimen (in MPa): **(a)** Distribution of $\sigma_h = \sigma_{11} + \sigma_{22}$ (reference solution), **(b)** Distribution of average Σ_h^{a1} (obtained with a small collimator with irradiated area 3×3 mm) and **(c)** Distribution of average Σ_h^{a2} (obtained with a large collimator with irradiated area 5×5 mm). The spatial step is $\Delta x = 0.1$ mm

$$\mathbf{R}^+ = (\mathbf{R}^T \mathbf{R})^{-1} \mathbf{R}^T. \quad (18)$$

In practice the pseudo-inverse \mathbf{R}^+ is calculated numerically using efficient algorithms based on using its singular-value decomposition (SVD). In both cases (underdetermined or overdetermined system), the method will provide a unique reconstructed stress field from several sets of measurements.

Application to the Reconstruction of Local Residual Stress Maps from Simulation Results

The aim of this section is to assess the deconvolution method in a reference case in which local residual stress field is known. Hence, the method is applied to the reconstruction of the local residual stress field determined numerically by FEM; the 2D moving averages are simply calculated from the local distribution of residual stresses. We consider the repetitive corrugation and straightening (RCS) process which is an interesting problem for the reconstruction as it can induce very heterogeneous surface residual stresses [17].

Description of Processing By Repetitive Corrugation and Straightening

Repetitive corrugation and straightening is a repetitive process for sheets, which consists of two steps (see Fig. 2):

1. An initial flat sheet is corrugated using two corrugation dies. This induces high shear deformation in the sheet. At the end of this step, the specimen is no longer a sheet as its shape is corrugated.
2. The corrugated specimen is then straightened using two flat straightening dies. At the end of this step, the specimen is again a flat sheet.

These two steps correspond to a *pass*. Interestingly, the specimen is almost flat at the end of a pass, so it is possible to repeat these passes in order to increase the shear deformation, which can be used to improve the mechanical properties [19]. As shown in [20] (see also [8, 17]), heterogeneous residual stresses are observed at the specimen surface after one pass.

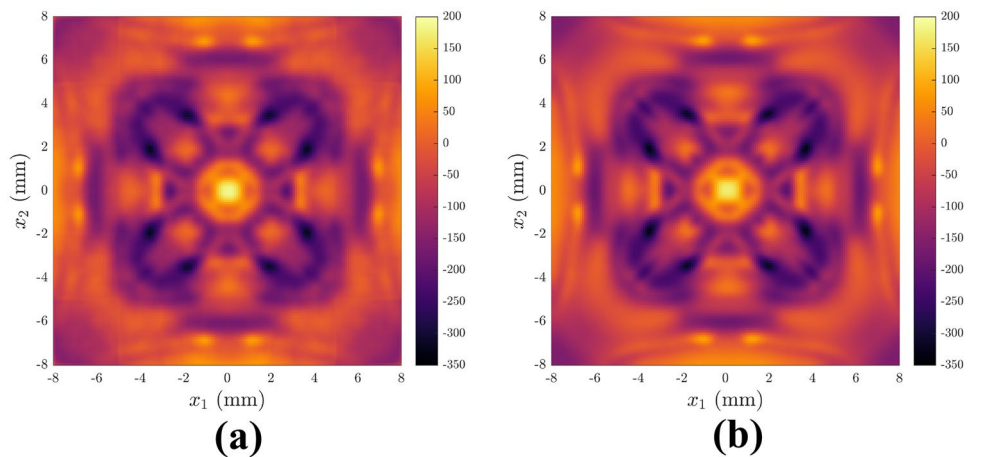
In this work we consider the two steps of the first pass of the process, consisting of one corrugation followed by a straightening, following the conditions given in [8]. The die profile is based on two perpendicular sinusoidal functions of period 16 mm, which is suitable for a sheet thickness of about 1 mm, so the size of an elementary pattern is $16 \times 16 \times 1$ mm (see Elizalde et al. [20]). We consider only one elementary pattern subjected to symmetric-periodic boundary conditions which is representative of a central pattern of the multi-pattern process [21]. The corrugation dies and straightening plates are rigid and the sheet is deformable. The mesh is composed of 11,664 linear R3D8 elements for each straightening plate, 13,568 R3D8 elements for each corrugation die and 256,000 C3D8R elements for the sheet (see Fig. 2). The size of an element in the sheet is $0.1 \times 0.1 \times 0.1$ mm.

In terms of material modelling we consider the case of a precipitation-hardened aluminum alloy 6061 whose behavior follows a power-law isotropic hardening; the yield stress σ_Y is given by

$$\sigma_Y = (\sigma_0 + hp^n), \quad (19)$$

where σ_0 is the initial yield stress, h the hardening modulus, n the hardening exponent and p the accumulated plastic strain. The material constants are given in Table 1. The contact between the dies and the test sample is supposed to follow a Coulomb model. The value $\mu = 0.25$ is chosen for the friction coefficient, which is typical for the aluminum-steel pair [8].

Fig. 4 Results of the reconstruction in the case of a fine spatial step ($\Delta x = 0.1$ mm) and no noise: (a) Reconstructed field and (b) Reference solution (for comparison)



After convergence of the calculation, we extract the distribution of the bi-axial stress $\sigma_h = \sigma_{11} + \sigma_{22}$ on the bottom surface of the specimen, which will constitute the reference stress distribution for the deconvolution method (see Fig. 3(a)). This quantity σ_h is considered in these simulations because it will be compared to the experimental results of "Application to the reconstruction of local residual stress maps from X-ray diffraction measurements", for which we measured σ_h ; indeed, the bi-axial stress can be measured by XRD with only one Ψ -angle as it is directly related to

the strain ε_{33} (see Appendix 2), which allows a fast mapping. In order to generate the average datasets mimicking XRD measurements, we consider two different collimator sizes representative of laboratory X-ray beams, a small one corresponding to an irradiated area of width $2a_1 = 3$ mm and a large one corresponding to an irradiated area of width $2a_2 = 5$ mm. Each dataset is defined in the interval $[-L/2 + a, L/2 - a]$ (with $L = 16$ mm) because the collimator cannot scan the entire domain due to the size of the irradiated area. These two sets of average are calculated on the

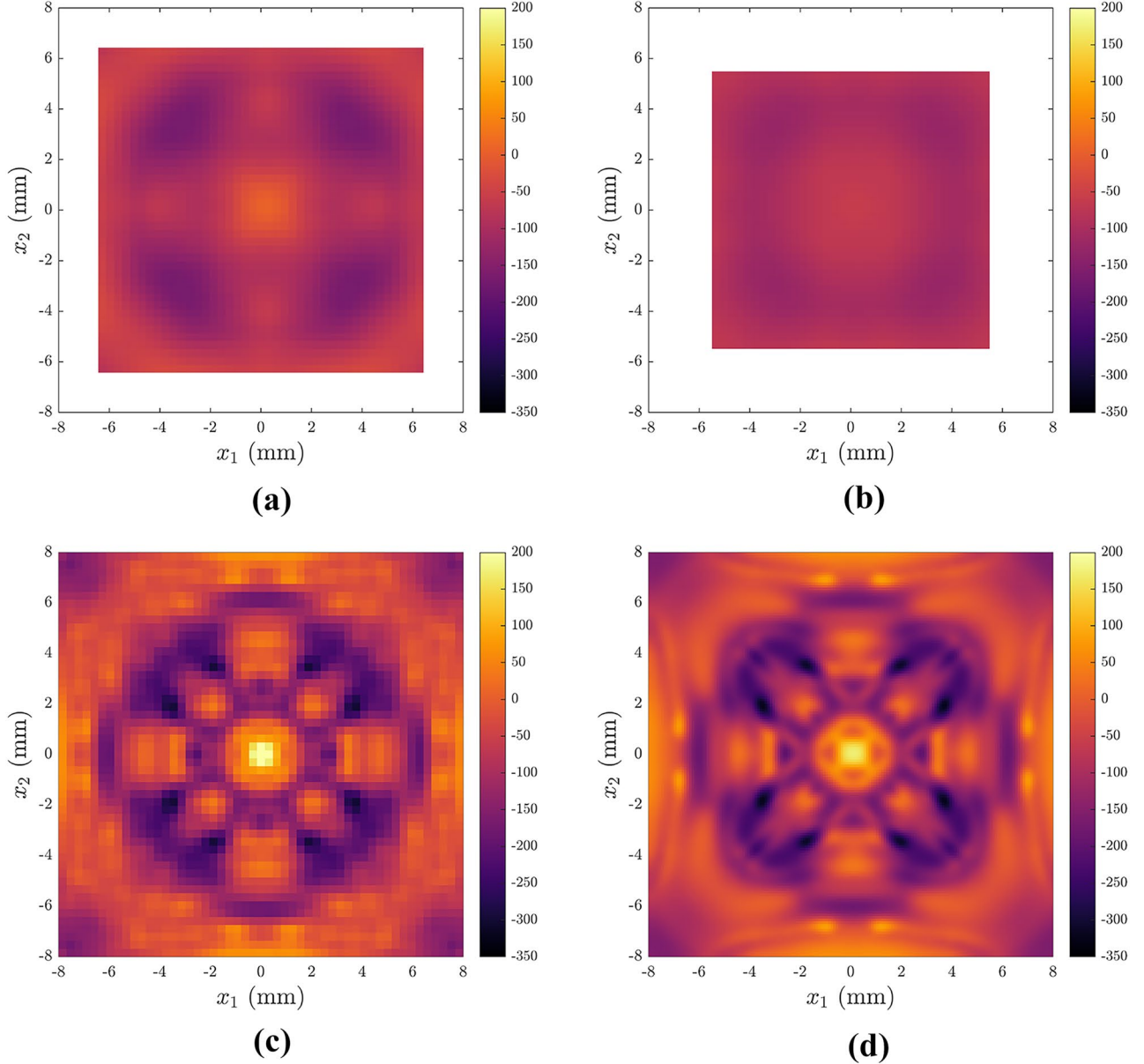
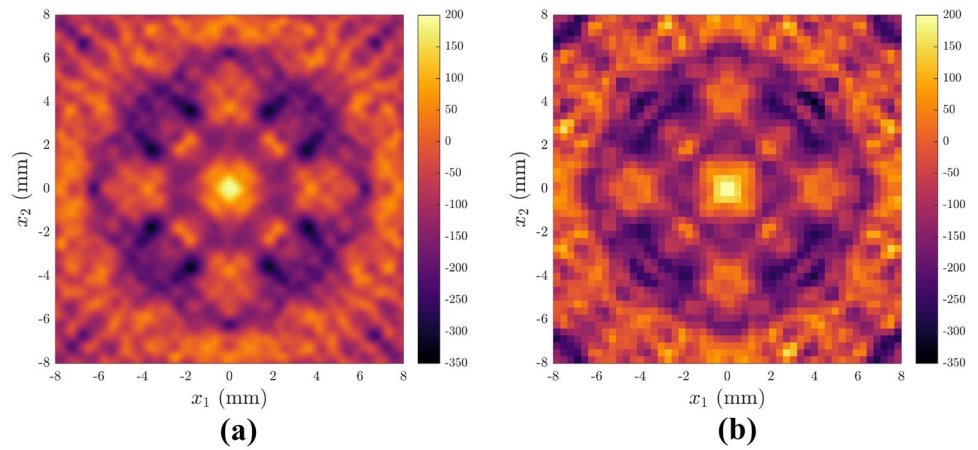


Fig. 5 Results of the reconstruction in the case of a coarse spatial step ($\Delta x = 0.32$ mm) and no noise: (a) Distribution of the average $\Sigma_h^{d_1}$ (obtained with a small collimator with irradiated area 3×3 mm) on the coarse grid, (b) Distribution of the average $\Sigma_h^{d_2}$ (obtained with a large collimator with irradiated area 5×5 mm) on the coarse grid, (c) Reconstructed field on the coarse grid and (d) Reference solution on the fine grid (for comparison)

Fig. 6 Results of the reconstruction in presence of noise ($\bar{\delta} = 10$ MPa). **(a)** Reconstructed field using a fine spatial step and **(b)** Reconstructed field using a coarse spatial step



initial mesh and will be used and post-treated as an input for the reconstruction (see Figs. 3(b) and (c)). In order to assess the quality of the reconstructed residual stress field, we will notably study the influence of (i) the spatial step Δx and (ii) noise on the average datasets.

Influence of the Spatial Step

The spatial step Δx is an important parameter in the experimental procedure as it is related to the precision of the experimental facility. Furthermore, a small spatial step would require a large number of experimental points and therefore increase the experimental time. Therefore, the study of the spatial step upon the reconstruction is important. Two cases are considered, a ‘fine’ spatial step $\Delta x = 0.1$ mm, which corresponds here to the smallest possible value as it coincides with the element size of the FEM calculation,

and a ‘coarse’ spatial step $\Delta x = 0.32$ mm which is typical for the experimental facility at the PIMM laboratory.

Fine spatial step ($\Delta x = 0.1$ mm) We begin with the fine spatial step $\Delta x = 0.1$ mm which corresponds to 161×161 ‘measurement’ points (i.e. 25921 points). The grid considered corresponds to the mesh so the average datasets collected directly corresponds to the distributions represented in Figs. 3(b) and (c). The average dataset corresponding to the small collimator is composed of 131×131 points and the average dataset corresponding to the large collimator is composed of 111×111 points; the matrix \mathbf{R} defining the linear system (14) is thus of size 29482×25921 and its rank can be estimated as 21201 (which is lower than 25921). The linear system is thus underdetermined but its rank has been improved by considering two datasets instead of only one. In this case since there is no noise on the dataset, the smooth datasets coincide exactly with the datasets constructed from

Table 2 Composition of the Al-6061 alloy

Element	Si	Fe	Cu	Mn	Mg	Cr	Zn	Ti	Al
wt%	0.77	0.24	0.16	0.03	1.03	0.07	0.03	0.02	balance

Fig. 7 Description of the specimen processed by a one pass RCS

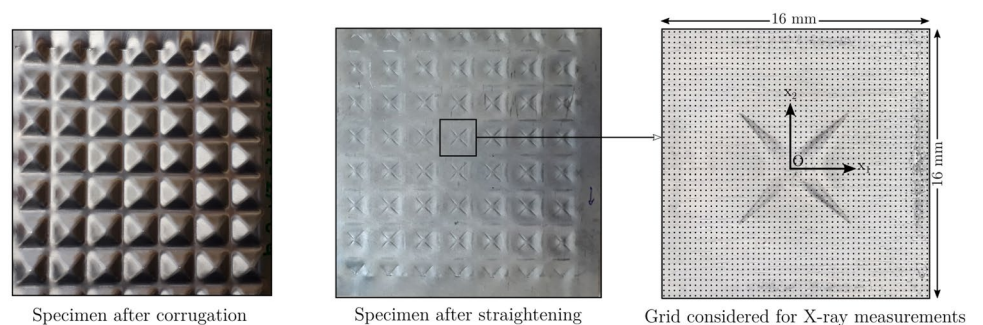
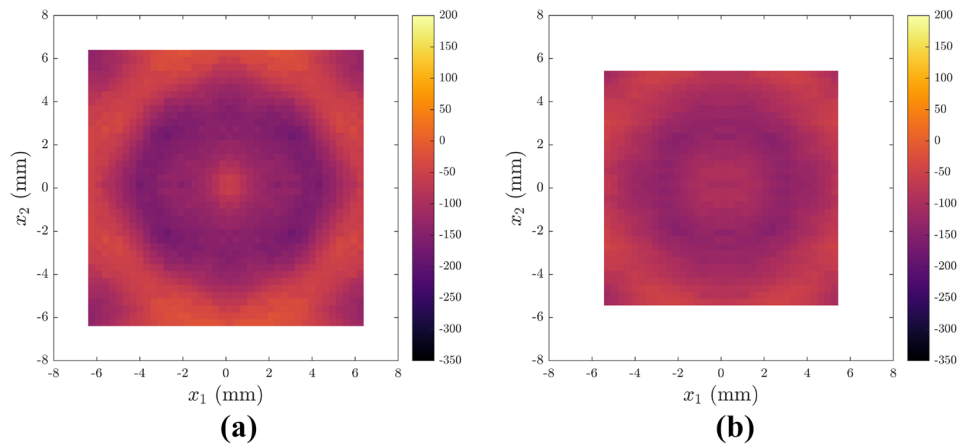


Table 3 Experimental conditions of X-ray diffraction

Cr-K α radiation	Voltage	Current	XRD planes	Angle 2θ	Ψ angles
0.2290 nm	20 KV	1 mA	(3 1 1)	139°	1 angle (0°) or 13 in $[-37.27^\circ, 39.23^\circ]$

Fig. 8 Distribution of the residual stress $\sigma_h = \sigma_{11} + \sigma_{22}$ (in MPa) determined experimentally by XRD. (a) Experimental results with a small collimator and (b) Experimental results with a large collimator



the FEM results. The reconstructed field is represented in Fig. 4(a). It coincides almost exactly with the reference solution (represented for comparison in Fig. 4(b)), emphasizing that the deconvolution method provides a very accurate reconstruction on a fine grid and without noise on the average datasets. This result is in agreement with [17]’s results on a line profile.

Coarse spatial step ($\Delta x = 0.32$ mm) Then we continue with the coarse spatial step $\Delta x = 0.32$ mm, corresponding to 51×51 ‘measurement’ points (i.e. 2601 points). The average data sets are simply taken from an interpolated grid constructed from the reference averages of the 161×161 grid. The average dataset corresponding to the small collimator, represented in Figs. 5(a), is composed of 41×41 points, and the average dataset corresponding to the large collimator, represented in Figs. 5(b), is composed of 35×35 points. The matrix \mathbf{R} defining the linear system (14) is thus of size 2906×2601 and its rank can be estimated as 2177 (which is lower than 2601 so the system is underdetermined). The reconstructed field is represented in Fig. 5(c). The comparison with the reference solution is good, considering that the grid is coarser than that of the reference case. The main features of the reference solution are reproduced, that is the ‘star’ shape of the stress distribution. The location and the level of the maximum and minimum values of the stress are also reproduced, emphasizing that the method can reasonably provide the shape and range of the residual stress distribution even with a coarse measurement grid.

Influence of Additional Noise

In practice, XRD measurements are collected with some noise, whose amplitude depends on the experimental conditions (such as the acquisition duration, the type of material, etc.). Therefore, it is interesting to study the influence of noise on the reconstructed field in this reference numerical case. Uniformly distributed numbers δ (with zero mean) are randomly generated in the interval $[-\bar{\delta}, \bar{\delta}]$ and added to the average stress distribution datasets Σ_h^a in order to mimic experimental noise:

$$\Sigma_{h,\text{noisy}}^a(x, y) = \Sigma_h^a(x, y) + \delta, \quad \delta \in [-\bar{\delta}, \bar{\delta}]. \tag{20}$$

In the following, the value $\bar{\delta} = 10$ MPa will be considered, which is typical of the experimental uncertainties observed in XRD laboratory conditions when aluminum alloys are investigated. We investigate the two cases (fine and coarse spatial step), although the study of the effect of noise is more relevant for the coarse spatial step since this case is closer to the real experimental conditions.

In the case $\Delta x = 0.1$ mm (fine spatial step), the reconstructed stress field is represented in Fig. 6(a). Overall, the reconstructed field is very close to the reference solution: the main features of the local stress field, in terms of location and magnitude, are reproduced up to some local fluctuations related to the presence of noise.

In the case $\Delta x = 0.32$ mm (coarse spatial step), the reconstructed stress field is represented in Fig. 6(b). In that case,

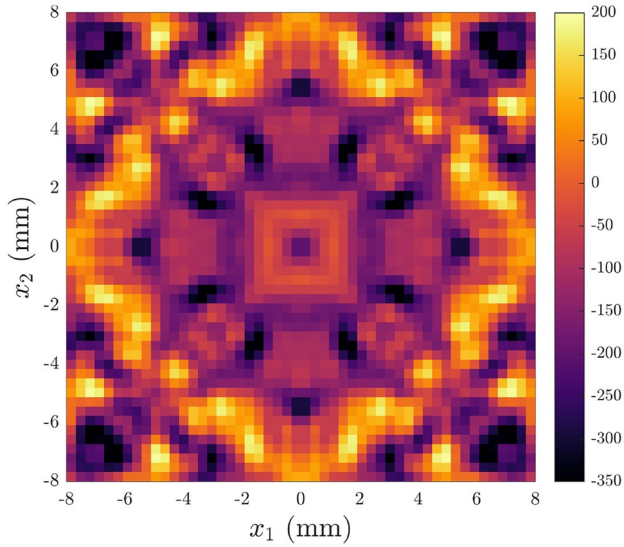


Fig. 9 Reconstructed residual stress distribution $\sigma_n = \sigma_{11} + \sigma_{22}$ (in MPa) from experimental XRD measurements

there are more discrepancies between the reference solution and the reconstructed field but the location and magnitude of the local stress are qualitatively well reproduced. The reconstructed solution improves significantly the prediction of residual stresses in this problem, as it is closer to the reference solution than the average datasets. Interestingly, the reconstructed solution with noise is in good agreement with the reconstructed solution without noise on the same grid ($\Delta x = 0.32$ mm) represented in Fig. 5.

Discussion

Overall, the deconvolution method provides accurate results in comparison with the reference solution. These results show that the quality of the reconstructed field depends mainly on two parameters, (i) the spatial discretization of the grid and (ii) the experimental noise on the average datasets. The consequence of noise on the average datasets is the occurrence of fluctuations on the reconstructed field, whose magnitude depends on the level of noise. The spatial discretization, on the other hand, has an influence on the stress gradients resolution that can be achieved. Stress gradients that occur at a smaller scale than the spatial step considered cannot be captured.

It is important to note that on a realistic case close to experimental conditions, i.e. with a spatial step $\Delta x = 0.32$ mm and a level of noise of $\bar{\delta} = 10$ MPa, the reconstructed field is in good agreement with the reference solution and improves the prediction of the residual stress field in comparison with the average datasets which exhibit important averaging effects.

Application to the Reconstruction of Local Residual Stress Maps From X-ray Diffraction Measurements

The deconvolution method is now applied to the reconstruction of residual stress mapping from experimental data, on a specimen processed by repetitive corrugation and straightening.

Description of the Experiments

We consider a precipitation-hardened aluminum alloy 6061 as in the numerical simulations of "[Application to the Reconstruction of Local Residual Stress Maps from Simulation Results](#)". A solid solution heat treatment at 803 K for two hours was applied, then the sample was water-quenched, followed by an aging treatment at 453 K for 18 h [20]. The chemical composition of the Al-6061 alloy is given in Table 2.

The AA-6061 sheets (of thickness 1 mm) are processed by repetitive corrugation and straightening at room temperature with a corrugation die based on two orthogonal sinusoidal profiles (see Elizalde et al. [20] for the design and machining of the sinusoidal RCS dies), as in "[Application to the Reconstruction of Local Residual Stress Maps from Simulation Results](#)". The die is composed of 7×7 elementary patterns of size 16×16 mm, so the size of the processed sheet is about $120 \times 120 \times 1$ mm (see Fig. 7). The RCS process is performed using a Instron 8802 servo-hydraulic testing system (250 kN). As in "[Application to the Reconstruction of Local Residual Stress Maps from Simulation Results](#)", only one pass is considered, that is a corrugation of an initial flat sheet followed by a straightening (see Fig. 7).

The residual stress distribution is evaluated on a central pattern located at the bottom surface of a one pass corrugated and straightened specimen, by X-ray diffraction measurements using the psi tilt method and an in-situ diffractometer type X-RAYBOT (manufactured by MRX France). The XRD measurements were performed with a spatial step 0.32 mm so the grid is composed of 51×51 points (i.e. 2601 points for the reconstructed field). We used two collimators, a small one with an irradiated area of size 3×3 mm, and a large with an irradiated area of size 5×5 mm, which permits to provide two average datasets requiring a total of 2906 measurement points. Due to the large number of measurement points required, the XRD measures have been performed using $\Phi = \Psi = 0^\circ$: this permits the determination of the strain ϵ_{33} which is related to the bi-axial

stress $\sigma_h = \sigma_{11} + \sigma_{22}$ at the surface (see [Appendix 2](#) for the details of the method). In addition, the full stress tensor is determined in several grid points (using 13 angles Ψ and 2 angles Φ) in order to determine the average of the free-stress interatomic lattice spacing d_0 . It should be noted that the full stress tensor could have been determined for all grid points but it would have increased by (at least) a factor 25 the experimental time, which was already very important using $\Phi = \Psi = 0^\circ$. The X-ray diffraction conditions are given in [Table 3](#).

Results

The two experimental average datasets determined by XRD are shown in [Figs. 8\(a\)](#) and [\(b\)](#). They consist of 41×41 measurement points for the small collimator and 37×37 measurement points for the large collimator. Since the die geometry is symmetric with respect to the x_1 -axis, x_2 -axis and the 45° -axes, the experimental data have been post-treated in order to enforce these symmetries, which allows the reduction of the experimental uncertainties. The effect of the collimator size is quite notable in terms of distribution and stress levels. For the small collimator, the stress is in the interval $[-180.1, -13.2]$ MPa and for the large collimator, the stress is in the interval $[-147.3, -43.8]$ MPa. Therefore, the stress gradients associated with the large collimator are smaller than that associated with the small collimator, which confirms that a notable averaging effect is induced by the measurement.

As in the case treated in "[Influence of the Spatial Step](#)", the matrix \mathbf{R} defining the linear system [\(14\)](#), associated with the coarse grid, is of size 2906×2601 and its rank is estimated as 2177: the linear system is thus underdetermined² but its rank has been improved by considering two datasets instead of only one. The residual stress distribution reconstructed is represented in [Fig. 9](#). The reconstructed distribution is considerably different from the average datasets collected experimentally. Very high stress gradients are predicted and some ‘star’ shape in the area deformed by the corrugated die are notably observed. In terms of stress levels, the stress is in the interval $[-415.4, 195.1]$ MPa. It is thus interesting to note that, in several areas, tensile stresses are observed on the reconstructed stress field while only compressive stresses were observed on the average datasets.

Interestingly, the distribution of the reconstructed stress field has similar features with that calculated numerically, although they do not coincide exactly. In the numerical simulation, the intervals of values for the stresses

are $[-321.6, 173]$ MPa for the reference distribution, $[-168.2, 9.8]$ MPa for the calculated small collimator average dataset and $[-125.4, -58.8]$ MPa for the large collimator average dataset. Very similar trends are observed between the experimental and numerical results in terms of distribution and magnitude of the local stress distributions as well as the average datasets, so it can be expected that the reconstructed experimental stress mapping is closer to the ‘real’ distribution than the average datasets. Hence, it can be reasonably assumed that the ‘real’ residual stress distribution is (i) significantly more heterogeneous than what we measured with the small and large collimators and (ii) has significantly higher compressive stresses and higher *tensile* stress.

Discussion

The local stress field reconstructed using the datasets collected from X-ray diffraction measurements with two collimators is very different than the two experimental datasets, which confirms that X-ray diffraction measurements induce strong averaging effects. In particular, high tensile stresses of about 195 MPa are observed on the reconstructed field, while the maximum values obtained experimentally are -13 MPa using the small collimator and -43.8 MPa using the large collimator. Moreover, since the distribution of experimental stress field reconstructed resembles that calculated numerically in similar processing conditions, it can be assumed that the 2D deconvolution method proposed in this paper has captured the essential features of the stress distribution. For this problem, the raw XRD measurements only provide compressive stresses, which seems unrealistic as tensile stresses were also predicted numerically. Hence, XRD measurements should always be compared to FEM calculations and, if possible, post-treated using the proposed deconvolution method in order to estimate the actual magnitude of the residual stress distribution. In the case where the residual stress field obtained by XRD measurements is used to calibrate some model parameters of a FEM calculation, it is necessary to take into consideration the spatial resolution of the measure and the averaging effects.

It should be noted that some small differences are still observed between the distribution of the numerical stress distribution and the experimental reconstructed one. Indeed, the numerical simulation of RCS has been performed with values of parameters that are difficult to measure experimentally, such as the friction coefficient and the applied forces of straightening plates. Hence, the processing conditions considered in the numerical simulation slightly differ from the experimental ones and no attempt was made to calibrate the process parameters, which can explain the discrepancies observed.

² It could be possible to improve the matrix’s rank by including another dataset with a different collimator size.

Conclusion

The objective of this work was to derive a deconvolution method for the reconstruction of heterogeneous residual stress mapping using X-ray diffraction measurements.

We extended Morin et al. [17]'s reconstruction method to a two dimensional case, by considering that averaging effects due to the irradiated area correspond to a convolution within a square-shaped domain. The combination of a fine measurement grid and the use of two collimators lead to an over-determined linear system between the point-wise values of the average datasets and the local stress field. The inversion of this linear system provides an estimate of the local residual stress field. The method has been first assessed in a reference case of repetitive corrugation and straightening, in which the solution has been computed numerically by the finite element method. The average datasets have been determined from the reference solution by mimicking XRD measurement, and used as an input for the deconvolution method. In a case close to experimental conditions (i.e. with a coarse measurement grid and additional noise), the method was shown to provide accurate results in terms of magnitude and location of the stress heterogeneities. The reconstruction technique has finally been applied to experimental X-ray diffraction data on a specimen processed by repetitive corrugation and straightening in conditions similar to the numerical simulations. Important averaging effects are observed on the datasets collected experimentally using two collimators. The reconstructed stress field has similar features with that calculated numerically, with notably local tensile stress which were not observed on the average datasets.

The present results confirm that residual stress distributions determined by X-ray diffraction are subjected to inherent averaging effects so that the measurements can be far from the exact local stress field in presence of high surface stress gradients due to the irradiated area. This can have important consequences upon the reliability of engineering components because the raw datasets obtained from XRD can ignore in some cases the presence of tensile stress due to the averaging effects. The deconvolution technique proposed allows a better reconstruction of local stress distributions which should improve (i) the assessment of engineering components by removing the averaging effects and (ii) the comparison between experimental results and numerical calculations.

Appendix 1

Robust Spline Smoothing of Noisy Data

In order to reduce the effect of noise in the inverse problem (14), smoothing splines are considered as a very efficient

technique to construct a smooth estimate $\tilde{\Sigma}^a$ of Σ^a by minimization of a functional \mathcal{G} that balances the fidelity to the data, through the residual sum-of-squares (RSS), and the smoothness of the estimate $\tilde{\Sigma}^a$, through some penalty term \mathcal{P} [18]:

$$\mathcal{G}(\tilde{\Sigma}^a) = \|\Sigma^a - \tilde{\Sigma}^a\|^2 + s\mathcal{P}(\tilde{\Sigma}^a). \quad (21)$$

In equation (21), $\|\cdot\|$ denotes the Euclidean norm and s is a real positive scalar that controls the degree of smoothing. The penalty term \mathcal{P} is defined from the point-values of the p -th derivative of $\tilde{\Sigma}^a$ at the grid points; in the case of the second-order derivative, it reads

$$\mathcal{P}(\tilde{\Sigma}^a) = \|\mathbf{D}\tilde{\Sigma}^a\|^2. \quad (22)$$

In the one-dimensional case, the differentiation matrix \mathbf{D} simply reads

$$\mathbf{D} = \frac{1}{\Delta x^2} \begin{pmatrix} -1 & 1 & \dots & 0 \\ 1 & -2 & 1 & \vdots \\ 0 & \ddots & \ddots & \ddots & 0 \\ \vdots & & 1 & -2 & 1 \\ 0 & \dots & & 1 & -1 \end{pmatrix}. \quad (23)$$

The minimization of \mathcal{G} leads to the expression of the smooth estimate $\tilde{\Sigma}^a$ [18]

$$\tilde{\Sigma}^a = \text{IDCT}(\Gamma(s) \circ \text{DCT}(\Sigma^a)), \quad (24)$$

where DCT and IDCT respectively refer to the discrete cosine transform and the inverse cosine transform, and \circ denotes Hadamard product (pointwise product). In the one-dimensional case, $\Gamma(s)$ is a vector whose components are given by

$$\Gamma_i = \frac{1}{1 + s\lambda_i^2}, \quad (25)$$

where the parameter λ_i is given by

$$\lambda_i = 2 - 2\cos\left(\frac{(i-1)\pi}{N-2k_a}\right). \quad (26)$$

The extension of the smoother to the two-dimensional case is straightforward [18]. The optimal smoother parameter s that avoids over- or under-smoothing is then estimated using the method of generalized cross-validation (GCV) introduced by [22]. The smoothing of the experimental data is thus fully automatic and the smoothing parameter estimate provided by the GCV method is unique [18, 23].

Appendix 2

Principles of XRD Measurements for a Fast Mapping of the Bi-axial Surface Stress

The principle of XRD measurements is to determine the interatomic spacing d of a family of diffracting planes using Bragg's law. If we denote by d_0 the free-stress interatomic lattice spacing, the strain is given by

$$\varepsilon_{\Phi\Psi} = \frac{d_{\Phi\Psi} - d_0}{d_0}, \quad (27)$$

where Φ and Ψ are the angles associated with the X-ray direction. In the case of an isotropic elastic material, it is straightforward to note that

$$\begin{aligned} \varepsilon_{\Phi\Psi} = & \frac{1+\nu}{E} (\sigma_{11}\cos^2(\Phi) + \sigma_{12}\sin(2\Phi) + \sigma_{22}\sin^2(\Phi) - \sigma_{33})\sin^2(\Psi) \\ & + \frac{1+\nu}{E}\sigma_{33} - \frac{\nu}{E}(\sigma_{11} + \sigma_{22} + \sigma_{33}) \\ & + \frac{1+\nu}{E}(\sigma_{13}\cos(\Phi) + \sigma_{23}\sin(\Phi))\sin(2\Psi). \end{aligned} \quad (28)$$

In the particular case $\Phi = 0^\circ$ and $\Psi = 0^\circ$, we have $\varepsilon_{\Phi=0^\circ, \Psi=0^\circ} = \varepsilon_{33}$, and therefore it is readily seen from equation (28) that

$$\varepsilon_{33} = \varepsilon_{\Phi=0^\circ, \Psi=0^\circ} = -\frac{\nu}{E}(\sigma_{11} + \sigma_{22}) + \frac{\sigma_{33}}{E}. \quad (29)$$

Since the XRD measurements are performed on the surface of normal e_3 , the normal stress σ_{33} is null. Using equations (27) and (29), the bi-axial stress σ_h finally reads

$$\sigma_h = \sigma_{11} + \sigma_{22} = -\frac{E}{\nu} \frac{d_{\Phi=0^\circ, \Psi=0^\circ} - d_0}{d_0}. \quad (30)$$

Consequently the determination of the interatomic spacing $d_{\Phi=0^\circ, \Psi=0^\circ}$ allows a fast mapping of the bi-axial stress σ_h since only one X-ray direction is required (with $\Phi = \Psi = 0^\circ$). In practice, the free-stress interatomic lattice spacing d_0 is also required; it is determined in several points of the specimen (by calculating the full stress tensor using for instance 13 angles Ψ).

Funding This work is supported by the Carnot Institut Arts. G.G. acknowledges UNAM-DGAPA-PASPA program for funding the sabbatical year at the UPV.

Declarations

Conflict of Interest The authors declare that they have no conflict of interest.

References

1. Webster GA, Ezeilo AN (2001) Residual stress distributions and their influence on fatigue lifetimes. *Int J Fatigue* 23:375–383
2. Vaara J, Kunnari A, Frondelius T (2020) Literature review of fatigue assessment methods in residual stressed state. *Eng Fail Anal* 110:104379
3. Nelson D (1981) Effects of residual stress on fatigue crack propagation. In: *Residual stress effects in fatigue*, ASTM STP 776. American Society for Testing and Materials Edition
4. Mahmoudi AH, Ghasemi A, Farrahi GH, Sherafatnia K (2016) A comprehensive experimental and numerical study on redistribution of residual stresses by shot peening. *Mater Des* 90:478–487
5. Peyre P, Fabbro R (1995) Laser shock processing: a review of the physics and applications. *Opt Quant Electron* 27:1213–1229
6. Ben Rhouma A, Sidhom N, Makhlof K, Sidhom H, Braham C, Gonzalez G (2019) Effect of machining processes on the residual stress distribution heterogeneities and their consequences on the stress corrosion cracking resistance of AISI 316L SS in chloride medium. *Int J Adv Manuf Technol* 105:1699–1711
7. Leggatt RH (2008) Residual stresses in welded structures. *Int J Press Vessel Pip* 85:144–151
8. Ezequiel M, Figueroa IA, Elizalde S, Cabrera JM, Braham C, Morin L, Gonzalez G (2020) Numerical and experimental study of a 5754-aluminum alloy processed by heterogeneous repetitive corrugation and straightening. *J Mater Res Technol* 9:1941–1947
9. Fang Z-C, Wu Z-L, Huang C-G, Wu C-W (2020) Review on residual stress in selective laser melting additive manufacturing of alloy parts. *Opt Laser Technol* 129:106283
10. Rossini NS, Dassisti M, Benyounis KY, Olabi AG (2012) Methods of measuring residual stresses in components. *Mater Des* 35:572–588
11. Lu J (1996) *Handbook of measurement of residual stresses*. Fairmont Press
12. Baczmanski A, Braham C, Seiler W, Shiraki N (2004) Multi-reflection method and grazing incidence geometry used for stress measurement by X-ray diffraction. *Surf Coat Technol* 182:43–54
13. Marciszko M, Baczmański A, Braham C, Wróbel M, Wroński S, Cios G (2017) Stress measurements by multi-reflection grazing-incidence X-ray diffraction method (MGIXD) using different radiation wavelengths and different incident angles. *Acta Mater* 123:157–166
14. Kahloun C, Badawi P, Viaris de Lesegno (1994) P X-ray Analysis. The case of substantial stress gradients and strong heterogeneity. In: *Proceedings of the 4th International Conference on Residual Stresses, Proceedings of the 4th International Conference on Residual Stresses*. Baltimore, Maryland, USA
15. Hennion V, Sprael JM, Michaud H (2000) Contribution to residual-stress evaluation in high-stress-gradient zones by X-ray diffraction. *J Appl Crystallogr* 33:26–34
16. Kahloun C, Badji R, Queyreau S, Franciosi P, Bacroix B (2014) Spatial convolution of a stress field analyzed by X-Ray diffraction. *Adv Mater Res* 996:169–174
17. Morin L, Braham C, Tajdary P, Seddik R, Gonzalez G (2021) Reconstruction of heterogeneous surface residual-stresses in metallic materials from X-ray diffraction measurements. *Mech Mater* 158:103882
18. Garcia D (2010) Robust smoothing of gridded data in one and higher dimensions with missing values. *Comput Stat Data Anal* 54:1167–1178
19. Huang J, Zhu YT, Alexander DJ, Liao X, Lowe TC, Asaro RJ (2004) Development of repetitive corrugation and straightening. *Mater Sci Eng A* 371:35–39

20. Elizalde S, Ezequiel M, Figueroa IA, Cabrera JM, Braham C, Gonzalez G (2020) Microstructural evolution and mechanical behavior of an Al-6061 alloy processed by repetitive corrugation and straightening. *Metals* 10:489
21. Tajdary P, Morin L, Braham C, Gonzalez G (2021) A reduced single-pattern model for the numerical simulation of multi-pattern metal forming. *Int J Mater Form* 14:1403–1416
22. Craven P, Wahba G (1978) Smoothing noisy data with spline functions. *Numer Math* 31:377–403
23. Garcia D (2011) A fast all-in-one method for automated post-processing of PIV data. *Exp Fluids* 50:1247–1259

Publisher's Note Springer Nature remains neutral with regard to jurisdictional claims in published maps and institutional affiliations.